Ewald sphere correction for single-particle electron microscopy

Matthias Wolf[a], David J. DeRosier[a], Nikolaus Grigorieff[a,b,*]

[a]Rosenstiel Basic Medical Sciences Research Center, Brandeis University, 415 South Street, Waltham, MA 02454, USA
[b]Howard Hughes Medical Institute, Brandeis University, 415 South Street, Waltham, MA 02454, USA

Abstract

Most algorithms for three-dimensional (3D) reconstruction from electron micrographs assume that images correspond to projections of the 3D structure. This approximation limits the attainable resolution of the reconstruction when the dimensions of the structure exceed the depth of field of the microscope. We have developed two methods to calculate a reconstruction that corrects for the depth of field. Either method applied to synthetic data representing a large virus yields a higher resolution reconstruction than a method lacking this correction.
© 2005 Elsevier B.V. All rights reserved.

1. Introduction

The three-dimensional (3D) reconstruction of a biological molecule or complex from images of single, isolated particles is an important step in electron microscopy (EM) of macromolecules. The reconstruction algorithms commonly used assume that the images are projections of the three-dimensional (3D) object. Although this assumption is a valid approximation for many situations, it breaks down when the size of the object and the desired resolution exceed the depth of field of the microscope [1]. The present work describes two methods to accommodate the depth of field in the reconstruction and alignment of single particles without the use of tilt or defocus pairs. We demonstrate the validity of the approach using simulations.

2. Theory

2.1. Ewald construction

A 3D reconstruction algorithm can be understood most easily by considering its action in reciprocal space. The Fourier transform of the data from each image does not correspond to a plane through the origin (central section) but rather to the surface of the Ewald sphere (EWS, [2]) that passes through the origin of the 3D Fourier transform. The construction in Fig. 1 shows that the deviation, Δz, between the sphere and a plane increases with increasing resolution (determined by the length of the vector g). The value of the Fourier transform of the object differs between the two points B, where the transform is sampled, and B′, where the data corresponding to a projection lies; the larger the difference, the greater the deviation of the image from a projection. The magnitude of the difference depends on the dimensions of the object and is larger for objects having a longer dimension along the beam direction.

The error made in the reconstruction when using the planar approximation depends, therefore, on the resolution, the size of the object, and the radius of the EWS (the wavelength of the radiation). DeRosier [1] performed an analysis of the expected phase error between B and B′ and showed that a phase error of 66° for the planar approximation of a spherical shell, such as a virus, occurs at a resolution $R = \sqrt{2 \times 0.7/(t\lambda)}$ (0.7 is a dimensionless empirical factor for a spherical shell, object diameter t and wavelength λ are given in units of Å) [1]. For example, for a virus of 500 Å diameter and a wavelength of 0.025 Å

*Corresponding author. Tel.: +1 781 736 2444; fax: +1 781 736 2419.
E-mail address: niko@brandeis.edu (N. Grigorieff).
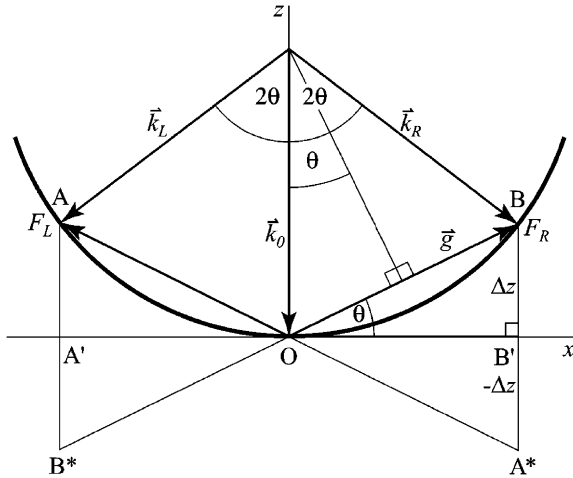
Fig. 1. Represents a slice through the 3D transform along the $x-z$ plane. An incident beam along the z-axis is scattered by the object, which emits two symmetrically scattered beams at scattering angles 2θ. The center of the EWS lies back along the beam direction by a distance of $1/\lambda$ from the origin of the reciprocal space coordinate system. The EWS surface represents all possible elastically scattered (diffracted) waves. The amplitude and phase of the Fourier transform at the position k correspond to the amplitude and phase of the wave scattered in the direction k. Waves scattered by the same angle 2θ are represented by a pair of left and right scattered waves, k_L and k_R. The scattered waves are recombined by the objective lens of the electron microscope and form an image by interference between each other and the unscattered beam. The amplitude and phase that are recovered from the image and that correspond to the scattering angle 2θ are a linear combination of F_L and F_R, the Fourier components for the left and right beam, respectively. If Δz is small, then F_L and F_R are Friedel related; that is, they are complex conjugates of one another. In this case, F_L and F_R can be recovered. At sufficiently high resolution, Δz is large enough that F_L and F_R are not related and cannot be recovered from a single image.

(200 kV electrons), $R = 1/3.0\,\text{Å}^{-1}$. At lower resolution, the errors are smaller but still significant.

2.2. Measured data

2.2.1. Beam combination

The two beams scattered at the angle 2θ are combined by the objective lens of the microscope, which causes them to interfere with the unscattered beam in the image plane. Assuming a thin specimen (a weak phase object), the scattering can be described as

$$\frac{A_t}{A_0} \approx 1 - i\rho(x) \tag{1}$$

(e.g. [3]). In the image, the combination (F_{obs}) of the Fourier coefficients of the right (F_R) and left (F_L) beam, modified by the contrast transfer function (CTF) of the lens, is recorded (Fig. 1). As derived by DeRosier [1], the resulting real (R_{obs}) and imaginary (I_{obs}) parts of the Fourier transform of the image are

$$R_{\text{obs}} = (R_R + R_L)\sin\chi + (I_R + I_L)\cos\chi,$$
$$I_{\text{obs}} = -(R_R - R_L)\cos\chi + (I_R - I_L)\sin\chi. \tag{2}$$

R_R and R_L are the real parts of F_R and F_L, respectively, whereas I_R and I_L are their imaginary parts. Eq. (2) can be rewritten as

$$F_{\text{obs}} = -iF_R\,e^{i\chi} + \left[-iF_L\,e^{i\chi}\right]^*. \tag{3}$$

* indicates the conjugate complex operation. χ describes the CTF of the microscope (e.g., [5,6]):

$$\chi = \frac{\pi C_S \lambda^3 g^4}{2} - \pi\,\Delta f\,\lambda \cdot \boldsymbol{g}^2, \tag{4}$$

where C_S is the third-order spherical aberration coefficient, Δf the change in focal length or defocus of the lens (a positive value corresponds to underfocus) and $\boldsymbol{g}$ the scattering vector.

Eqs. (2) and (3) describe the phase contrast in an image. Usually, an image also contains amplitude contrast that arises from electrons lost to the elastic image by their inelastic scattering or scattering outside the aperture. The amplitude contrast is introduced into the scattering formula by an "absorption" term α:

$$\frac{A_t}{A_0} \approx 1 - (i + \alpha)\rho(x) \tag{5}$$

(e.g. [3]). By analogy to Eq. (3), F_{obs} becomes

$$F_{\text{obs}} = -(i + \alpha)F_R\,e^{i\chi} + \left[-(i + \alpha)F_L\,e^{i\chi}\right]^*, \tag{6}$$

where

$$R_{\text{obs}} = [R_L + R_R + \alpha(I_L + I_R)]\sin\chi$$
$$+ [I_L + I_R - \alpha(R_L + R_R)]\cos\chi,$$
$$I_{\text{obs}} = [I_R - I_L + \alpha(R_L - R_R)]\sin\chi$$
$$+ [R_L - R_R + \alpha(I_L - I_R)]\cos\chi, \tag{7}$$

Thus we have two observations R_{obs} and I_{obs}, but four unknowns R_L, I_L, R_R, and I_R. DeRosier [1] suggested several methods for obtaining additional data to solve for all four unknowns. The new methods we have developed are modified versions of the algorithm incorporated in *FREALIGN* [4]. In *FREALIGN*, the Fourier transform data from the images are inserted into the 3D Fourier transform of the reconstruction by generating a set of Fourier coefficients on the corresponding 3D lattice. In the algorithm the cloud of observed Fourier coefficients that surrounds each lattice point is summed using weighting functions to approximate the value of the unknown Fourier coefficient at the lattice point.

2.3. Modifications of the FREALIGN method

The first modification to the *FREALIGN* insertion algorithm concerns the location of the observed Fourier coefficients. Because of the curvature of the EWS, the data correspond to the points A and B, not A' and B' (Fig. 1). Moreover, the two beams are not Friedel mates but are at least partially independent and can have different amplitudes and phases. 3D reconstruction is performed by inserting the data for each particle image into the correct
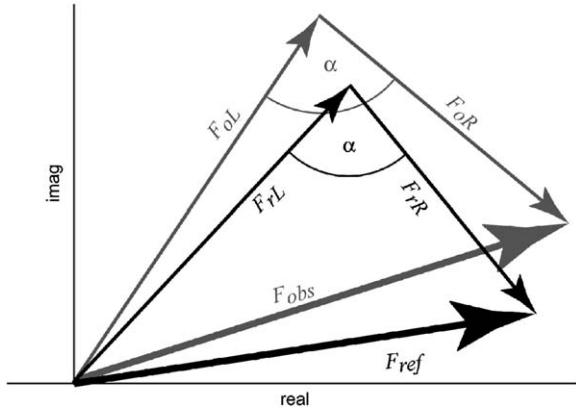
Fig. 2. An Argand diagram showing how the 3D reference map is used to split the observed data.

Fig. 3. Ewald construction for an image of an object, and for a second image of the object flipped 180° around an axis perpendicular to the beam. If these two images were strict projections (flat EWS) they would be related by a mirror. The same pair of images could, therefore, also be generated by an object with opposite handedness. However, due to the EWS curvature, the two images are not related by a mirror. Hence, an object with opposite handedness would not generate the same pair of images. In the diagram, the Fourier components are related diagonally, since these are Friedel mates (R_R, I_R, R_L, I_L are the real and imaginary parts of the right and left beam).

coordinates in Fourier space [4] along the EWS. The problem is how to separate the two image components that correspond to the left and the right side of the EWS.

We investigated two methods of including the observed data. The first method simply includes F_{obs} twice at the correct locations (i.e., at A and B instead of A′ and B′) of the reconstruction. We will refer to this method as the simple insertion method. F_{obs} contains the unseparated contributions from both beam components F_R and F_L. At point B, for example, the component F_R is included correctly but the other, F_L, is not and has the effect of adding extra noise. The second method uses a reference from a previous reconstruction cycle to split the image data into the two components for the right and left beam (Fig. 2). We will refer to this method as the reference-based insertion method. The observed Fourier component F_{obs} is the sum of components of the right and left beam F_{oR} and F_{oL}. The corresponding Fourier component F_{ref} from the reference map is the sum of the right and left coefficients, F_{rR} and F_{rL}. F_{oR} and F_{oL} are chosen such that the relative angle α between them is the same as that between F_{rR} and F_{rL}, and the ratio of their amplitudes is the same as the ratio of the amplitudes of F_{rR} and F_{rL}. This is achieved by setting

$$F_{oR} = (F_{rR} \times F_{obs})/F_{ref} \qquad (8)$$

and

$$F_{oL} = (F_{rL} \times F_{obs})/F_{ref}. \qquad (9)$$

Repetition of this procedure with the resulting reconstruction as a new reference will minimize the difference vector.

A third possibility to separate the contributions of the left and right beams in Fig. 1 is illustrated in Fig. 3. For this method we assume we have two images of the same object at the same defocus, which differ in their orientation by 180°. As shown in Fig. 3, the Fourier components of the two opposing views are related to each other, leading to a system of equations that allows solving for the left and right components. However, in practice it is difficult to find image pairs in the particle stack that show exactly opposite views of the particle. In the special case of a particle with a

two-fold axis in the plane of the image, the image would represent both opposing views of the particle and the Fourier components could be extracted directly. However, in general, even with a large number of randomly oriented particles the accuracy of the determined orientation would become the limiting factor. Therefore, this approach was not pursued further.

2.4. CTF correction

If the first method of EWS correction is used (simple insertion method with inclusion of F_{obs} twice at the correct locations in the 3D Fourier transform), CTF-corrected coefficients $F_{3D,k}$ at lattice points k of the 3D Fourier transform of the structure can be calculated as

$$F_{3D,k} = \frac{\sum_{j,s} w_{js}^2 c_{js} F_{obs,js}}{f + \sum_{j,s} (w_{js} \operatorname{Re}(c_{js}))^2}. \qquad (10)$$

The sums in Eq. (10) run over all images j and points s within each image Fourier transform that are close to lattice point k. w_{js} is a weighting term that includes the interpolation function used to approximate the Fourier terms on the 3D lattice, as well as weights characterizing the quality of the image. c_{js} represents the CTF term and is set to $[-(i + \alpha) e^{i\chi}]^*$ for the insertion of F_{obs} on the right side, and $-(i + \alpha) e^{i\chi}$ for the insertion of F_{obs} on the left side. f is a Wiener filter constant. At low resolution, the two insertion points (A and B in Fig. 1) are Friedel mates, points A^* and B (A and B^*) coincide, and the two inserted terms add to give $F_{obs} \operatorname{Re}(c_{js})$. The real part of c_{js} is simply given by $\sin \chi - \alpha \cos \chi$ [5,6], and Eq. (10) becomes the

same formula as previously described for the reconstruction algorithm without EWS correction [4]. At higher resolution, points A and B are no longer related, and the result of Eq. (10) will differ from that derived previously in Ref. [4].

Using the second (reference-based) method, $F_{3D,k}$ is given by

$$F_{3D,k} = \frac{\sum_{j,s} w_{js}^2 \operatorname{Re}(c_{js})^2 F_{o,js}}{f + \sum_{j,s}(w_{js} \operatorname{Re}(c_{js}))^2}. \tag{11}$$

F_o is either the right (F_{oR}) or left (F_{oL}) beam component of F_{obs} calculated in Eqs. (8) and (9), depending on which component is close to lattice point k and included in the sum. In Eq. (11) the CTF term acts only as a weighting term and does not change the phase of F_o since the phase is already corrected by the division by F_{ref} in Eqs. (8) and (9).

2.5. Handedness of the structure

The handedness of the structure is important when considering the EWS. If the image were a true projection, there would be no way of detecting the hand of the structure without using some additional technique such as tilting the structure in the microscope. When the EWS is taken into account, however, this ambiguity is removed. If $O(\mathbf{r})$ is the density of the object, then $\bar{O}(\mathbf{r}) = O(-\mathbf{r})$ has the opposite handedness. Accordingly, in Fig. 1, F_R and F_L have to be replaced by F_R^* and F_L^*, respectively. Hence, for the observed image $\bar{F}_{obs}$ of the inverted structure

$$\bar{F}_{obs} = -(i + \alpha)F_R^* \, e^{i\chi} + \left[-(i + \alpha)F_L^* \, e^{i\chi} \right]^*. \tag{12}$$

The inversion of the object leads to an apparent $180°$ rtation of the observed image along the image plane, compared with the image of the non-inverted object. To compare the two images, we rotate the image $\bar{F}_{obs}$ by another $180°$ and obtain

$$\bar{F}_{obs}^{180} = \bar{F}_{obs}^* = (i - \alpha)F_R \, e^{-i\chi} + \left[(i - \alpha)F_L \, e^{-i\chi} \right]^* \tag{13}$$

and

$$\begin{aligned} \bar{R}_{obs} &= [R_L + R_R - \alpha(I_L + I_R)]\sin\chi \\ &\quad - [I_L + I_R + \alpha(R_L + R_R)]\cos\chi, \\ \bar{I}_{obs} &= [I_R - I_L - \alpha(R_L - R_R)]\sin\chi \\ &\quad - [R_L - R_R - \alpha(I_L - I_R)]\cos\chi. \end{aligned} \tag{14}$$

Eqs. (13) and (14) describe the observed image of an object of opposite handedness to that described by Eqs. (6) and (7). If the EWS curvature is neglected, $F_L = F_R^*$ and $\bar{F}_{obs}^{180} = F_{obs} = 2F_R[\sin\chi - \alpha\cos\chi]$ which leads to the ambiguity in the handedness described above.

In an experimental case where the handedness of the object is unknown, the difference between Eqs. (6) and (13) can be used as a test to determine the handedness. If the object is small or the resolution is not very high, the difference will be small and difficult to detect. However, for larger objects, such as viruses, and higher resolution,

correlation coefficients can be calculated between observed images and images calculated from a reference structure using either (6) or (13). Provided that none of the observed images were mirrored during scanning or image processing, the average correlation coefficients for the entire data set should differ significantly between the two cases, identifying the correct handedness as that corresponding to the higher correlation. It is thus, in principle, possible to determine the absolute handedness of an object from a single image. In practical terms, however, averaging of many images is required to recover sufficient signal from the noisy data.

3. Tests of the methods using simulated images

An artificial 3D test object consisting of a synthetic virus with an average diameter of about $500\,\text{Å}$ diameter was created. Two sets with 2000 images of the object were calculated using an effective electron beam at $200\,\text{kV}$ (see Section 6). One set contained strict projections, and one set contained images calculated taking the curvature of the EWS into account; that is, the Fourier coefficients of the first set were extracted from the 3D transform from a central section along a plane "planar-extracted images" while in the second set they were taken along the surface of the EWS "Ewald-extracted images". Each set was subsequently used to generate 3D reconstructions using one of the two methods we proposed. Icosahedral symmetry was then imposed on the reconstruction. The success of the method was monitored using the Fourier Shell Correlation (FSC) generated by comparing the Fourier coefficients of the reconstruction to those of the synthetic virus (i.e., the true values).

Fig. 4 shows the FSC as a function of resolution for the first method we propose, which simply inserts F_{obs} twice at the correct locations of the reconstruction. As a control, we took the images corresponding to true projections and inserted the data as the appropriate central sections. The resulting Fourier coefficients are essentially perfect out to the Nyquist limit as expected for the control (see curve PP, Fig. 4). Next, using the data generated from images which included curvature of the EWS, we inserted the data not as a planar section but at the point on the EWS from where they originated when calculating the images. The result (curve E+E+, Fig. 4) is almost as good as the result above, thus showing that the algorithm corresponding to the first proposed method works. For comparison, we also tried some other combinations. If we took data that included curvature of the EWS but treated it as if it were from a true projection (planar insertion), the resolution was noticeably worse (curve E+P). The same loss occurred if the data corresponding to perfect projections was used as if it needed to be corrected for curvature of the EWS (curve PE+). Finally, when using data that included curvature of the EWS but assumed the wrong hand (that is, with the EWS center on the other side of the central plane), we found that the resolution is considerably worse (curve
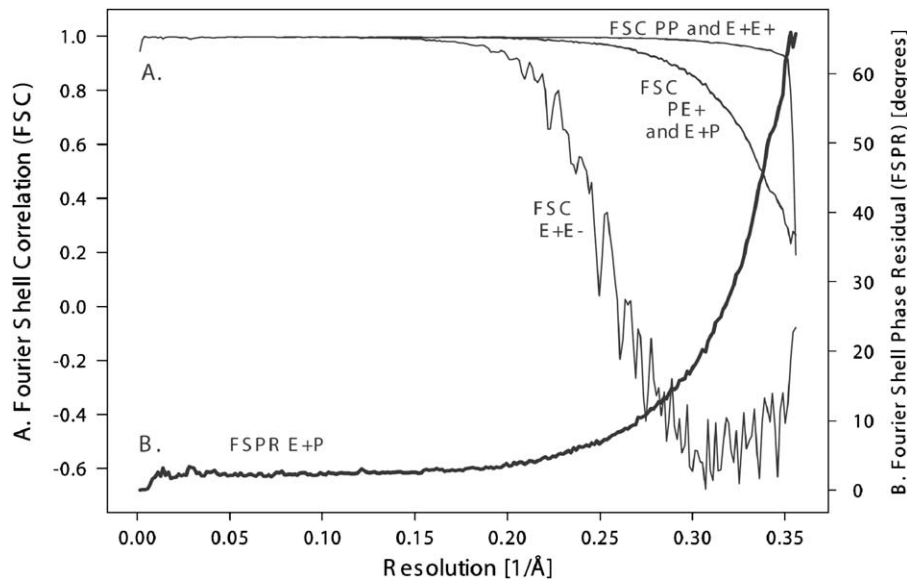
Fig. 4. Noise-free data and simple insertion method: (A) Fourier shell correlations (FSC, left ordinate) between a synthetic 3D reference and its reconstruction with and without EWS correction from 2000 simulated images of a synthetic virus with an average diameter of 500 Å at 200 kV. The images were generated once by extraction of the Fourier coefficients along a planar central section through the 3D transform of the reference "planar extraction" and once by extraction of the Fourier coefficients lying on the surface of the "EWS extraction" in the 3D transform. *Top coinciding pair of thin curves*: planar extraction and reconstruction by planar insertion (PP). EWS extraction and reconstruction by EWS insertion (E + E +). Both methods reproduce the original faithfully across most of the spectrum. The extra noise added by the EWS insertion methods does not produce a noticeable difference in the FSC curve in this case because the signal-to-noise ratio of the reconstruction remains high despite the added noise, giving correlation coefficients close to 1. *Middle coinciding pair of thin curves*: EWS extraction and reconstruction by planar insertion (E + P). Planar extraction and reconstruction by EWS insertion (PE +). If the data is not corrected for EWS curvature, there is an increasing phase error which deteriorates the reconstruction at high resolution. *Bottom thin curve*: EWS extraction and reconstruction by insertion of the image Fourier components along an EWS of opposite curvature (E + E−); this shows the effect of getting the hand of the structure wrong. If the curvature of the EWS is opposite to that of the data, then the effect of EWS "correction" results in a worse reconstruction than if uncorrected. (B) *Thick curve*: Fourier shell phase residual (FSPR, right ordinate) between E + P and the original model: a phase error of 66° is reached at 2.8 Å.

E + E−). This last result is expected to be the worst because it places the data twice as far from the place at which it was extracted. Finally, we also plotted the Fourier Shell Phase Residual (FSPR, [7]) between the reconstruction calculated by planar insertion from images that included EWS curvature, and the original synthetic structure. This curve can be compared with curves plotted in Ref. [1]. A phase error of 66° is reached at 2.8 Å, close to the resolution of 3 Å predicted in Ref. [1] for a 500 Å shell (see above).

Under noise-free conditions, both simple and reference-based insertion methods perform perfectly; there is essentially no difference between these two methods (Fig. 5, top dashed pair of curves). Two additional sets of images were generated that were identical with the first two sets but contained added noise at an overall signal-to-noise ratio of 0.1 (see Section 6). A signal-to-noise ratio of 0.1 falls into the range of experimentally observed values, based on correlation coefficients we observe between low-dose images of viruses and a high-resolution reference (data not shown). Under noisy conditions, as the signal becomes weak towards high resolution, the reference-based method yields a lower FSC, even when using the original model as a reference.

We then asked if a cycle of refinement might improve the resulting reconstruction. To test this idea, we took the reconstructions (E + E + and reference method) generated

in the first round and used them as the references in a second round of the reference-based method. The resulting maps were both slightly worse.

Why does the second, reference-based method not work as well as the simple insertion method? The model-derived information used by our reference-based insertion algorithm is the relative angle between the two beams and the ratio between the two beam amplitudes. With a perfect reference, F_{obs} is split correctly. However, the noise term in F_{obs} is also split and scaled. Setting $F_{obs} = F + N$ for the signal and noise term, we have for the right beam, $F_{oR} = [F_{rR} \times (F + N)]/F_{ref}$. If F_{ref} happens to be small the noise term will be strongly enhanced. The same is true for the left beam F_{oL}. The noise amplification might be the reason why the reference-based method falls behind the simple method when used with noisy data.

4. Discussion

The EWS construction and its effects on images in transmission EM have been discussed previously [8–10], most recently by DeRosier [1]. DeRosier also provided algorithms to take the EWS curvature into account in the 3D reconstruction of macromolecular complexes. While there is a relatively straight-forward implementation of an algorithm that deals with helical objects and 2D crystals,
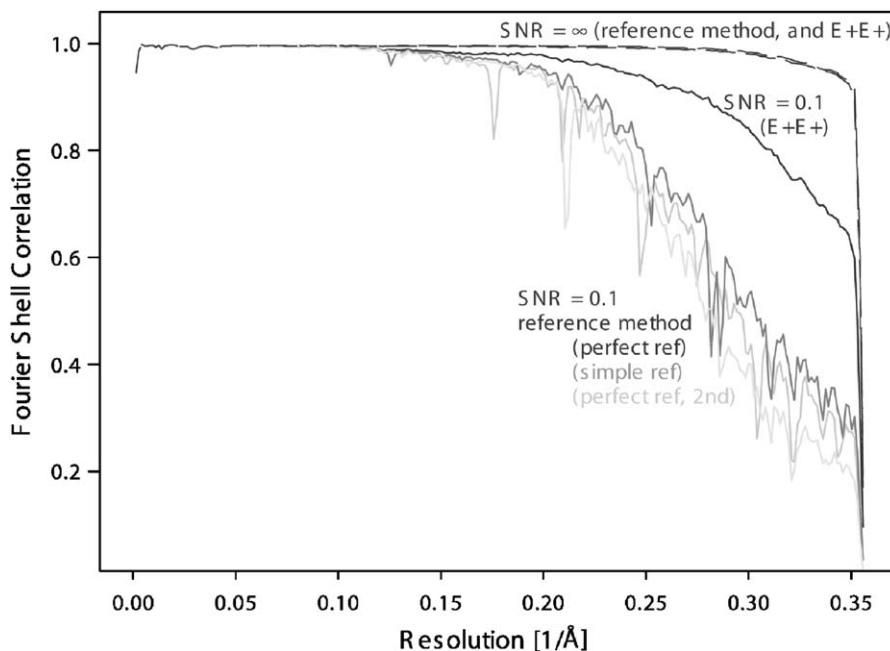
Fig. 5. Performance evaluation of both insertion methods with synthetic data under noise free conditions (top dashed pair of curves, SNR = ∞) and at image signal-to-noise ratios (SNR) of 0.1 (solid curves). The FSC is calculated between original reference and reconstructions from 2000 simulated images of a synthetic virus at 200 kV. The EWS corrected reconstruction by simple insertion of images extracted along the EWS of the original under noisy conditions represents the benchmark "E + E + ". This reconstruction or the original reference was subsequently used as a model to derive the splitting of the two beams during insertion ("simple ref" or "perfect ref."). Whereas both simple and reference-based methods of insertion work flawlessly under noise free conditions, the reference-based algorithm falls short under noisy conditions: EWS corrected reconstruction using the original reference as a model "SNR = 0.1, perfect ref." and subsequent reconstruction using this previous reconstruction as a reference "SNR = 0.1, perfect ref., 2nd" or reconstruction using the previous result of the simple method as a model "SNR = 0.1, simple ref.".

the implementation described for single-particle structures involved the recording of defocus pairs for each particle. Defocus pairs provide the necessary information to correctly retrieve the structure of the object. In theory, this procedure is superior to the algorithms described here because an incorrect addition of some Fourier components of the image (simple insertion method) or iteration (reference-based method) is avoided. However, the recording of defocus pairs doubles the number of images that need to be collected and processed for a given project, and it adds an additional source of error because the defocus difference between the two images in a pair is often not precisely known.

Our simulations using a structure derived from an atomic model of HPV with an average diameter of 500 Å show that the resolution in a reconstruction would be limited to about 3 Å if the EWS curvature is ignored (Fig. 4B). In most single-particle projects, a 3 Å resolution is not yet reached and the EWS curvature does not impose a serious limitation. However, for larger objects, such as the double-stranded DNA containing paramecium *Bursaria chlorella* virus type 1 (PBCV-1, 1900 Å diameter) [11] and Chilo iridescent virus (CIV, 1850 Å diameter) [11], the limiting resolution would be about 6 Å (assuming a 200 kV electron beam) and the algorithms described here would be key to reaching higher resolution. Other examples are clathrin-coated pits [12]. Potential applications of the new algorithms would also include electron tomographic data.

It has been argued that the resolution in the *z*-dimension of a tomogram cannot exceed twice the section thickness [13]. This is due to incomplete sampling leading to a missing cone of data, but also due to the lack of defocus correction which proves difficult for tilted specimen. Typical cryo sections have a thickness of 300–800 nm [14] and the field of view can span several microns across the tomographic section. The effective height of a sample measuring 5 μm across is about 43,000 Å at a tilt of 60°, limiting the resolution of the reconstruction to 25 Å at 300 kV due to the effect of the EWS curvature alone. While the correction of the EWS curvature in tomographic reconstructions would solve the problem of correcting for the defocus gradient, the problems associated with the missing cone of data, radiation damage and multiple scattering remain.

5. Conclusions

We have described two methods for EWS correction of structures derived using single-particle EM that do not require multiple exposures of the same object at different defocus or tilt. Tests with synthetic data generated using a virus with about 500 Å diameter show that the final reconstruction reaches higher resolution using the new algorithms than a reconstruction without EWS correction. The correction requires knowledge of the correct handedness of the object. The new algorithms have been implemented in the program *FREALIGN* [4].

6. Methods

A complete atomic model of HPV16 in its $T = 7$ form was created by the Scripps VIPER icosahedral server [15] applying the coordinates of the HPV16 capsid model (Protein Data Bank (PDB) entry: 1LOT) derived from the crystal structure of a small virus-like particle of the L1 protein by Modis et al. [16]. The electron density map was generated with the program *pdb2mrc* [17] with heteroatoms in a $512 \times 512 \times 512$ pixel volume at 1.4 Å/pixel and a resolution of 2.8 Å. To create simulated projections, a separate program was written called *MODEL* using the projection algorithm implemented in *FREALIGN* [4].

A set of 2000 noise-free projections was created from the test object by extraction of the data along central sections of the Fourier transform of the test volume, using random Euler angles and with subsequent multiplication by the CTF using a range of defoci, including amplitude contrast. A second set of noise-free images was generated in a similar way, but by extraction of the data along the surface of the EWS and combining the two Fourier components of the right and left beam according to Eq. (8). A third and fourth data set were created in identical manner as the two previous ones, but with a $SNR = 0.1$ (variance ratio) by adding Gaussian-distributed noise to the images. Image creation and processing parameters for all four data sets were: magnification 50,000 ×, acceleration voltage 200 kV, $C_S = 2.0$ mm, amplitude contrast 7%, pixel size 1.4 Å, defocus range 5000–45,000 Å on 50 different micrographs.

3D density maps were reconstructed with the program *FREALIGN* [4] from single-particle images of each test data set, using the list of rotational, translational, and defocus parameters generated upon test set creation. Image data were inserted into the 3D Fourier transform either as planar sections or along the curvature of the EWS. The FSC and FSPR between different volumes were calculated with the THREED-COMPARE command implemented in the software *IMAGIC* [18]. The data were plotted with *SIGMAPLOT 2001* [19]. All calculations were performed on personal computers with Intel® dual Xeon® processors or AMD® Athlon® processors running under the Linux operating system. *FREALIGN* was compiled with Portland Group® Fortran 5.2 (PGF77) to enable the processing of $512 \times 512 \times 512$ pixel volumes on 32-bit Linux.

References

[1] D.J. DeRosier, Ultramicroscopy 81 (2000) 83.
[2] P.P. Ewald, Ann. Phys. (Leipzig) 64 (1921) 253–287.
[3] J.M. Cowley, Diffraction Physics, Elsevier, Amsterdam, 1995.
[4] N. Grigorieff, J. Mol. Biol. 277 (1998) 1033.
[5] H.P. Erickson, A. Klug, Philos. Trans. Roy. Soc. Lond. B 261 (1971) 105.
[6] R.H. Wade, Ultramicroscopy 46 (1992) 145.
[7] M. Van Heel, Ultramicroscopy 21 (1986) 95.
[8] H.A. Cohen, M.F. Schmid, W. Chiu, Ultramicroscopy 14 (1984) 219.
[9] W.O. Saxton, Ultramicroscopy 55 (1994) 171.
[10] P. Schiske, Fouth European Conference on Electron Microscopy, 1968, p. 145.
[11] X. Yan, N.H. Olson, J.L. Van Etten, M. Bergoin, M.G. Rossmann, T.S. Baker, Nat. Struct. Biol. 7 (2000) 101.
[12] A. Fotin, Y. Cheng, P. Sliz, N. Grigorieff, S.C. Harrison, T. Kirchhausen, T. Walz, Nature 432 (2004) 573.
[13] B.F. McEwen, M. Marko, Methods Cell Biol. 61 (1999) 81.
[14] R. Grimm, H. Singh, R. Rachel, D. Typke, W. Zillig, W. Baumeister, Biophys. J. 74 (1998) 1031.
[15] V.S. Reddy, P. Natarajan, B. Okerberg, K. Li, K.V. Damodaran, R.T. Morton, C.L. Brooks III, J.E. Johnson, J. Virol. 75 (2001) 11943.
[16] Y. Modis, B.L. Trus, S.C. Harrison, EMBO J 21 (2002) 4754.
[17] S.J. Ludtke, P.R. Baldwin, W. Chiu, J. Struct. Biol. 128 (1999) 82.
[18] M. van Heel, G. Harauz, E.V. Orlova, R. Schmidt, M. Schatz, J. Struct. Biol. 116 (1996) 17.
[19] D. Kornbrot, Br. J. Math. Stat. Psychol. 53 (Pt 2) (2000) 335.